Cell structure and heat release in aluminum air heterogeneous detonations

Pikai Zhang [1,*] Huangwei Zhang [2] and Zheng Chen [3]

[1]*Department of Chemical Engineering, KTH Royal Institute of Technology, Brinellvägen 8, 114 28 Stockholm, Sweden*

[2]*Department of Mechanical Engineering, National University of Singapore, 9 Engineering Drive 1, Singapore 117576, Singapore*

[3]*SKLTCS, HEDPS, College of Engineering, Peking University, Beijing 100871, China*

(Received 23 June 2026; accepted 28 October 2026; published 12 November 2026)

Aluminum (Al), owing to its high energy density and favorable storage characteristics, has been widely used in energetic materials and propulsion-related applications. Al-particle detonations involve strong coupling among shock compression, interphase transport, and particle surface reactions. In this study, two-dimensional simulations of Al–air heterogeneous detonations are performed using a two-way Eulerian–Lagrangian framework to examine the effects of off-stoichiometric particle loading, particle diameter, and longitudinal particle-loading modulation on cellular dynamics and heat-release pathways. For uniform particle distributions, fuel-lean and fuel-rich detonations exhibit distinct frontal structures. Under fuel-lean conditions, the induction and reaction zones remain relatively uniform, resembling gaseous cellular detonations. Under fuel-rich conditions, intense localized heat release develops along triple-point trajectories, whereas excessive particle accumulation behind the Mach stem suppresses surface reactions through strong convective heat absorption, leading to reduced stability. For nonuniform particle distributions, increasing the imposed loading wavelength enlarges and distorts the cellular structure, induces large-scale peak-pressure modulation, and promotes local reinitiation events. Larger particles and fuel-rich loadings amplify these destabilizing effects, while smaller particles and fuel-lean mixtures show greater resistance to loading-induced perturbations. These results clarify how particle response, interphase momentum loss, and localized surface reactions jointly control nonuniform Al–air heterogeneous detonation dynamics.

DOI: 10.1103/pxtc-m7bp

I. INTRODUCTION

Aluminum (Al) particle detonations are important in high-energy-density propulsion, energetic materials, and explosion safety [1,2], because Al provides high volumetric energy density and intense heat release during oxidation. In an oxidizing gas, detonation propagation in Al suspensions is controlled not only by gas-phase shock dynamics but also by gas–particle momentum exchange, particle heating, and surface reactions [3–5]. As a result, the propagation velocity, cellular structure, and stability depend sensitively on particle size, loading, and spatial distribution. Clarifying these effects is therefore essential for understanding the mechanisms governing heterogeneous detonation propagation in reactive gas–solid mixtures.

*Contact author: pikai@kth.se

Published by the American Physical Society under the terms of the Creative Commons Attribution 4.0 International license. Further distribution of this work must maintain attribution to the author(s) and the published article's title, journal citation, and DOI. Funded by Bibsam.

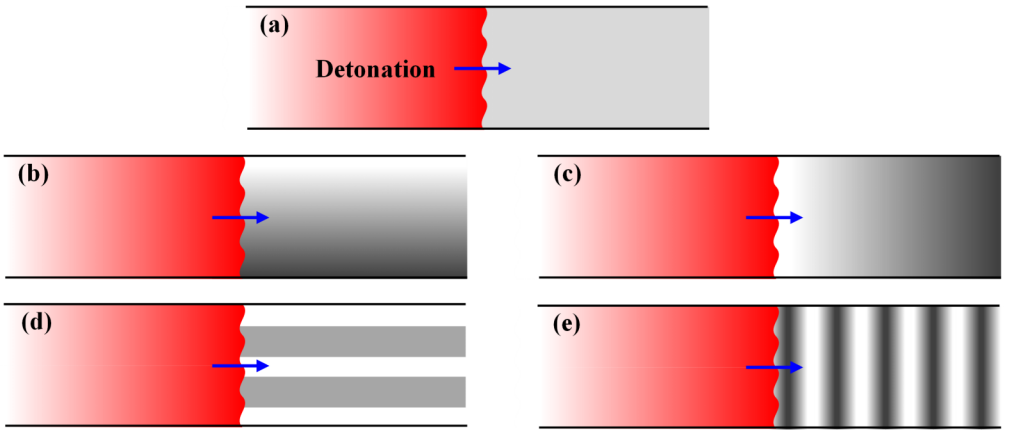


FIG. 1. Schematic of heterogeneous detonation propagating in (a) uniform and (b)–(e) nonuniform aluminum suspensions. The gray-to-black regions denote dispersed aluminum particles, with darker shades indicating higher particle concentrations.

In many studies of Al-particle cellular detonations (e.g., Refs. [5–7]), the particles are initially assumed to be uniformly distributed, as illustrated in Fig. 1(a). Under this configuration, particle loading plays a central role in determining detonation propagation and cellular structure. Near the detonation limits, Al–air detonations become particularly sensitive to deviations from stoichiometry [8]. The generalized multiphase C–J analysis by Zhang *et al*. [9] indicates that the detonation velocity reaches a maximum near the stoichiometric condition and decreases under both fuel-lean and fuel-rich conditions. Experimental measurements and numerical simulations have also shown that overly lean or overly rich Al-particle suspensions may approach failure or lose self-sustained propagation [8,10,11]. These off-stoichiometric conditions, especially when combined with spatial variations in particle loading, therefore provide a relevant configuration for examining cellular instability and localized energy release in heterogeneous detonations.

Even when the particles are initially uniform, however, the particle field can rapidly evolve into a highly nonuniform distribution after being swept by the leading shock. This redistribution is driven by particle inertia, gas–particle slip, and shock-induced flow structures [12–14], and is characteristic of heterogeneous dispersed-phase mixtures rather than single-phase gaseous detonations. It gives rise to distinctive phenomena, such as particle spike structures [6] and azimuthal detonative wavelets [15], which have no direct counterpart in purely gaseous detonations. Veyssiere *et al*. [16] and He *et al*. [6] further showed that heat release in Al–air detonations is strongly coupled with such inhomogeneous particle distributions: particles in relatively low-pressure or low-concentration regions may heat up and enter rapid combustion earlier, whereas high-concentration regions absorb more heat and exhibit delayed combustion. These findings indicate that, beyond the effect of mean particle loading, the spatial nonuniformity of the particle field can substantially modify shock–reaction coupling, transverse-wave dynamics, and cellular detonation behavior.

Several representative nonuniform particle distributions are summarized in Figs. 1(b)–1(e). For streamwise and transverse concentration gradients, as shown in Figs. 1(b) and 1(c), respectively, Khmel and co-workers [8,17,18] established a basic physical picture based on simulations of micron-sized Al/O_2 suspensions. Streamwise concentration gradients mainly alter the mean propagation velocity [8], whereas transverse gradients can fundamentally reorganize the cellular pattern by bending the leading front and producing oblique, strongly asymmetric cells [17]. In such flows, transverse-wave activity tends to intensify in particle-rich regions, while particle-lean regions exhibit larger cell spacing and weaker cellular activity. For layered configurations, as shown in Fig. 1(d), Afanasenkov *et al*. [19] demonstrated that the layer interface is intrinsically unstable

due to coupled Kelvin–Helmholtz and Richtmyer–Meshkov instabilities, with Kelvin–Helmholtz instability becoming dominant at high particle loadings. In comparison, periodic particle-loading modulation, as shown in Fig. 1(e), remains largely unexplored in heterogeneous detonations, although analogous periodic nonuniformities have recently received increasing attention in homogeneous gaseous detonations [20,21]. Such a configuration may also be relevant to rotating detonation engines, where fresh reactants are injected through discrete ports, and the unburned mixture may exhibit spatially periodic nonuniformity between discrete injection ports [22].

To address these issues, we conduct a numerical investigation of Al–air heterogeneous detonations under off-stoichiometric conditions, considering both uniform and longitudinally modulated particle distributions in a two-dimensional domain. A fully coupled Eulerian–Lagrangian framework is employed to resolve interphase mass, momentum, and energy exchange between the gas phase and Al particles. The analysis focuses on how off-stoichiometric particle loading and spatial nonuniformity affect the propagation characteristics, cellular dynamics, and heat release patterns of Al–air heterogeneous detonations. The objectives are twofold: (i) to clarify the distinct heat release mechanisms governing fuel-lean and fuel-rich detonations, and (ii) to quantify the effects of nonuniform particle loading on detonation cell size, reinitiation behavior, and pressure oscillations. The remainder of this paper is organized as follows. Section II describes the physical problem and numerical methodology. Section III presents the results and discussion for uniform and nonuniform particle distributions. Finally, Sec. IV summarizes the main findings.

II. PHYSICAL PROBLEM AND NUMERICAL METHODOLOGY

A. Physical problem

We first examine heterogeneous detonation propagation in air containing uniformly distributed aluminum particles under off-stoichiometric conditions. Two particle loadings, $\eta_0 = 50$ and $400\,\mathrm{g/m^3}$, are considered, corresponding to the equivalence ratios of $\Phi = 0.3$ and $\Phi = 2.7$, respectively. These loadings are selected based on the detonation limits predicted by the C–J curve of Zhang *et al*. [9]. The effects of nonuniform particle distributions, specifically longitudinal particle-loading modulation, on detonation propagation are then investigated. Figure 2(a) schematically shows the particle-loading profiles for the uniform and nonuniform distributions. In the detonation development section ($x<x_0$), the particles are uniformly distributed, allowing the detonation wave to develop into a quasisteady propagation state before entering the modulated-loading region. For the nonuniform section ($x>x_0$), the particle loading is prescribed as a sinusoidal function, i.e.,

$$\eta = \eta_0[\sin(2\pi(x - x_0)/\Lambda) + 1], \tag{1}$$

where η_0 denotes the reference mean loading, and Λ is the wavelength of the imposed modulation. Regions with $\eta > \eta_0$ are defined as high-loading regions (H), whereas regions with $\eta < \eta_0$ are defined as low-loading regions (L).

Figure 2(b) shows the two-dimensional computational domain and the prescribed nonuniform particle loading contours. The initial gas pressure and temperature are $p_0 = 0.5$ bar and $T_{c,0} = 300$ K, respectively. Three high-pressure and high-temperature hot spots are vertically placed near the left side of the domain to initiate the detonation, with an initial pressure of $100p_0$ and an initial temperature of 2500 K. A nonreflective condition is enforced for pressure, while zero-gradient conditions are imposed for other quantities. At the right boundary, zero-gradient conditions are applied to all variables. Periodic boundary conditions are used at the upper and lower boundaries. The Al particles are assigned a specific heat capacity of 890 J/kg/K and a material density of $2700\,\mathrm{kg/m^3}$. Several assumptions are made for the particle phase: (1) the particles are initially pure Al and monodisperse; (2) interparticle collisions are neglected because the maximum local particle volume fraction remains below approximately 0.5%; (3) the particle temperature is spatially uniform, which is justified by the small Biot number [23]; (4) the particles remain spherical throughout the combustion process; and (5) the Al_2O_3 produced by surface reactions remains attached to the particle surface.

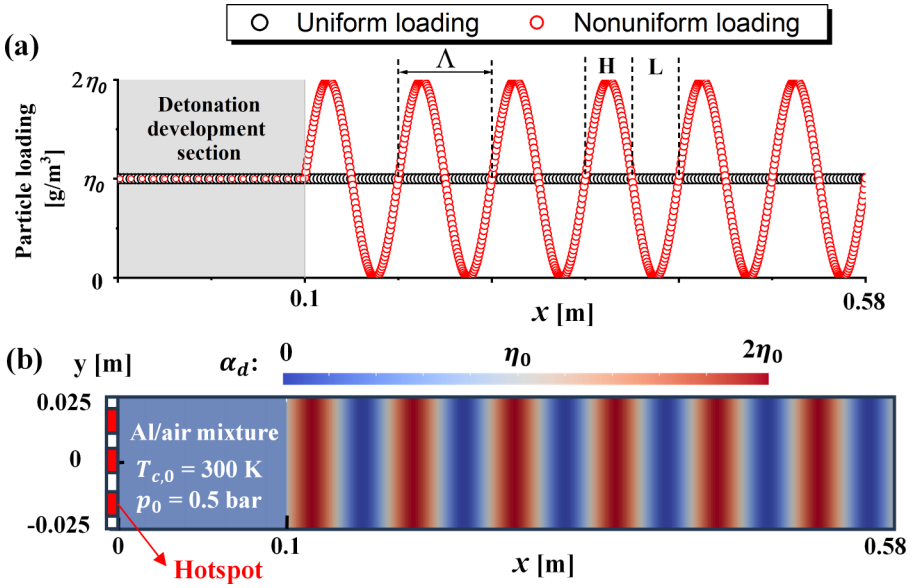


FIG. 2. (a) Particle loading profiles for the uniform and nonuniform distributions, where $\mathbf{\Lambda}$ denotes the imposed loading wavelength, and H and L indicate the high- and low-loading regions, respectively. (b) Schematic of the two-dimensional computational domain showing the initial nonuniform particle loading contours.

B. Numerical method

The two-phase compressible reacting flow is simulated using the *DSRYrhoCentralFoam* solver [24,25], in which the Eulerian gas phase and Lagrangian particle phase are coupled through the exchange of mass, momentum, and energy source terms at runtime. These source terms are evaluated using the particle-source-in-cell (PSI-CELL) method [26]. The solver has been extensively validated and applied to various two-phase detonation systems, including aluminum-hydrogen-air, coal-methane-air, and hydrogen-water-droplet mixtures [15,27,28]. Details of the governing equations are provided in Sec. A of the Supplemental Material [29], and only the key models are described below.

For particle motion, the improved drag model proposed by Loth *et al.* [30] is adopted. This model incorporates corrections for particle Reynolds number, Mach number, and Knudsen number effects, based on extensive experimental data and particle-resolved direct numerical simulations. It has been shown to be applicable to both incompressible and compressible flows, spanning continuum to rarefied particle regimes. Moreover, particle heat transfer is modeled using a modified Ranz–Marshall correlation [31], in which the convective heat-transfer coefficient is evaluated with Mach-number corrections. For particle surface reactions, the hybrid kinetic–diffusion model proposed by Zhang *et al.* [32] is employed. This model does not rely on a prescribed ignition temperature and has been widely used in Al particle detonation simulations [1,33,34]. It has been validated for highly transient processes, including detonation initiation and abrupt deflagration-to-detonation transition (DDT) [32]. The detailed formulations of these models are given in Sec. A of the Supplemental Material [29].

For the Eulerian gas equations, a second-order backward differencing scheme is employed for temporal discretization, and the time step is approximately 5×10^{-10} s. The convective fluxes in the momentum equations are calculated with a Riemann-solver-free MUSCL scheme [35] with a van Leer limiter, while the diffusion terms are solved with second-order central differencing. The Lagrangian particle governing equations are integrated with an implicit Euler method, while the

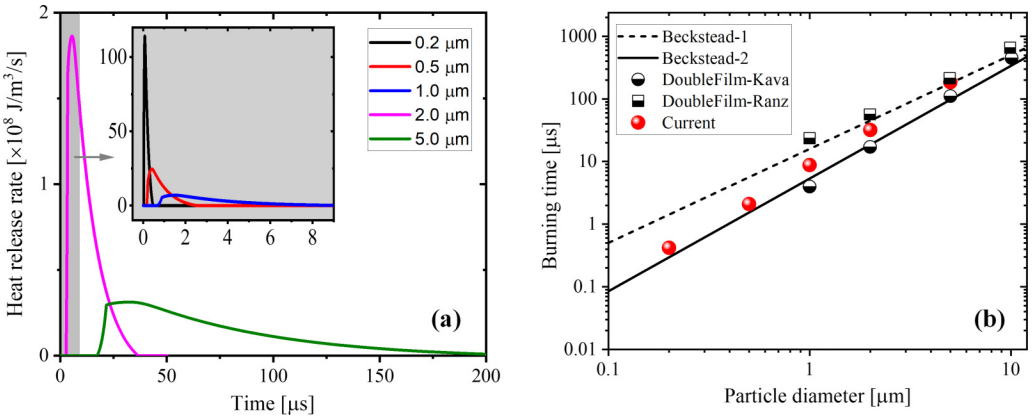


FIG. 3. Validation of the aluminum-particle combustion model. (a) Temporal evolution of the heat-release rate for single aluminum particles with different diameters; (b) comparison of the predicted particle burning times with the correlations of Beckstead [40] and the data reported by Zhang *et al*. [41].

source terms are handled in a semi-implicit way. Details about the numerical method can be found in Ref. [36].

Based on the simulated heat-release fields, the particle induction-zone length is estimated to be generally larger than 1.0 mm. With the adopted uniform grid size of 75 μm, this length is resolved by at least 13 grid points. Numerical soot foils, presented in Sec. B of the Supplemental Material [29], show that uniform Cartesian meshes with grid sizes of 37.5 and 75 μm yield comparable cellular regularity and characteristic cell size ($\lambda \approx 1.67$ cm at $\eta_0 = 50\,\mathrm{g/m^3}$). Therefore, a uniform Cartesian mesh with a cell size of 75 μm is used to discretize the entire computational domain, resulting in approximately 5.17 million cells. For the particle phase, a parcel concept is adopted [37,38], in which each computational parcel represents multiple physical particles with identical properties, such as diameter and temperature. The prescribed particle loading variation is achieved by varying the number of particles contained in each parcel. This parcel-based approach is widely used in Eulerian–Lagrangian simulations of two-phase flows to reduce computational cost while retaining the essential dynamics of the dispersed phase [39]. Except for the initial hot-spot region, one parcel is initialized in each computational cell, resulting in approximately 5.15 million parcels in total.

C. Solver validation and simulation cases

In this section, the single-particle combustion model is first validated under representative post-detonation conditions ($p = 10$ atm and $T = 2500$ K). Figure 3(a) presents the temporal evolution of the heat-release rate for Al particles with diameters ranging from 0.2 to 5.0 μm. With increasing particle diameter, the peak heat-release rate decreases significantly, whereas the burning duration becomes markedly longer. Here, the particle burning time is defined as the time interval between the two instants at which the heat-release rate reaches 5% of its peak value during the rising and decaying stages, respectively. The corresponding burning times are summarized in Fig. 3(b) and compared with the Beckstead correlations [40] and the data reported by Zhang *et al*. [41]. The present predictions reproduce the expected particle-size dependence and show reasonable agreement with the reference results over the entire diameter range considered.

The details of the simulated cases are summarized in Table I. Two particle diameters, 0.5 and 1.0 μm, are considered because micron- and submicron-sized Al particles are favorable for achieving sufficiently rapid heating, ignition, and energy release during detonation propagation [32,42]. For the uniform particle distributions, both fuel-lean ($50\,\mathrm{g/m^3}$, $\Phi = 0.3$) and fuel-rich

TABLE I. Summary of simulation conditions.

Distribution	η_0 [g/m^3] (Φ)	D_d [μm]	Λ [cm]
Uniform	50 (0.3)	1.0	N/A
Uniform	148 (1.0)	1.0	N/A
Uniform	400 (2.7)	1.0	N/A
Uniform	400 (2.7)	0.5	N/A
Nonuniform	50 (0.3)	1.0	2, 4, 6
Nonuniform	400 (2.7)	1.0	2, 4, 6
Nonuniform	400 (2.7)	0.5	2, 4, 6

(400 g/m^3, $\Phi = 2.7$) conditions are examined. For the nonuniform particle distributions, the effects of longitudinal particle-loading wavelength ($\Lambda = 2$, 4, and 6 cm) are investigated, including their influence on detonation propagation speed, cellular structure, and energy-release characteristics. This wavelength range corresponds to the centimeter-scale mixture inhomogeneities commonly observed near injection ports in laboratory-scale rotating detonation engines [43,44].

Figure 4 summarizes the measured detonation speeds in the Al–air and Al–oxygen mixtures, together with the equilibrium Chapman–Jouguet (C–J) predictions, as a function of equivalence ratio. The solid curve represents the equilibrium detonation velocity predicted by the generalized C–J model of Zhang *et al*. [9], in which the heterogeneous gas–particle mixture is treated as an equilibrium detonation system, and the shocked mixture reaches a final thermochemical equilibrium state at the sonic plane. The experimental data cover a broad range of equivalence ratios and provide

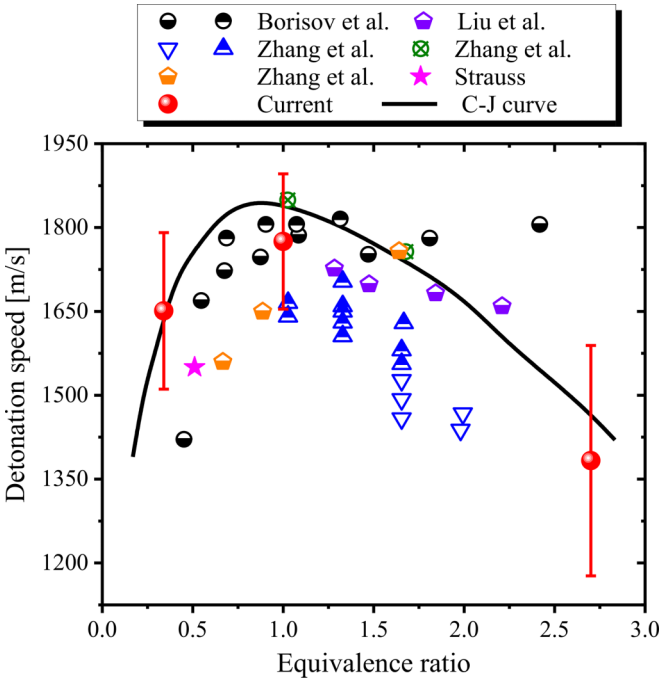


FIG. 4. Comparison of the present results with theoretical and experimental data. The C-J curve is from Zhang *et al*. [9]; the experimental data are from Zhang *et al*. [10,32,45], Borisov *et al*. [42], Liu *et al*. [46,47] and Strauss [48]. Error bars denote the RMS values of the detonation speed.

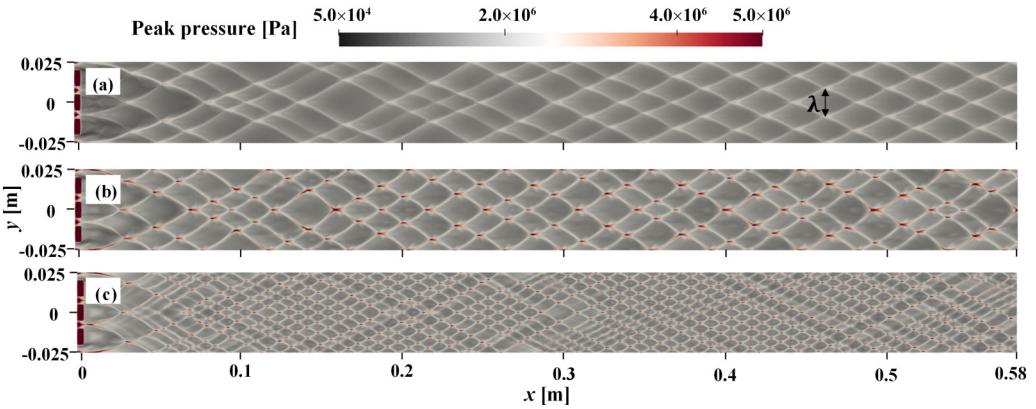


FIG. 5. Numerical soot foils (i.e., peak pressure history) for uniform particle loadings with: (a) $\boldsymbol{D_d} = 1$ μm, $\boldsymbol{\eta_0} = 50\,\mathrm{g/m^3}$ ($\boldsymbol{\Phi} = 0.3$); (b) $\boldsymbol{D_d} = 1$ μm, $\boldsymbol{\eta_0} = 400\,\mathrm{g/m^3}$ ($\boldsymbol{\Phi} = 2.7$), and (c) $\boldsymbol{D_d} = 0.5$ μm, $\boldsymbol{\eta_0} = 400\,\mathrm{g/m^3}$ ($\boldsymbol{\Phi} = 2.7$).

a reference for evaluating the detonation-speed variation under off-stoichiometric conditions. Deviations from the C–J curve are expected because real Al-particle detonations involve particle ignition delay, incomplete particle reaction, and wall losses.

For the current results, the streamwise evolution of the instantaneous detonation speed is provided in Sec. C of the Supplemental Material [29]. The predicted detonation speeds follow the same overall trend as the C–J curve and experimental data: the detonation speed is higher near $\Phi = 1.0$, whereas it decreases as the mixture deviates from stoichiometry. In particular, the error bars, representing the root-mean-square (RMS) values of the detonation speed, increase under strongly off-stoichiometric conditions, indicating enhanced propagation unsteadiness [6,8]. Overall, the comparison indicates that the present model can capture reasonably well the Al-particle detonation speed over a range of equivalence ratios.

III. RESULTS AND DISCUSSION

A. Uniform particle loading

1. Cellular morphology and propagation dynamics

Figure 5 presents the trajectories of the peak pressure ($p_{\max}$) for the three uniform-loading cases in Table I. Case A corresponds to $D_d = 1.0$ μm and $\eta_0 = 50\,\mathrm{g/m^3}$ ($\Phi = 0.3$), whereas Cases B and C correspond to a higher loading of $\eta_0 = 400\,\mathrm{g/m^3}$ ($\Phi = 2.7$), with particle diameters of 1.0 and 0.5 μm, respectively. Unlike in homogeneous gaseous detonations, the location of $p_{\max}$ in heterogeneous detonations does not necessarily coincide with the leading shock, but typically lags behind it by a finite distance because of gas-phase momentum loss induced by particle drag [3,49]. Nevertheless, the $p_{\max}$ trajectories still represent the triple-point paths and the resulting cellular structure. Figure 6 further shows the centerline ($y = 0$) evolutions of the detonation speed and leading-shock pressure for the three cases.

For Case A, with $D_d = 1.0$ μm and $\eta_0 = 50\,\mathrm{g/m^3}$, a relatively regular cellular structure is observed, with a characteristic cell width of $\lambda \approx 1.67$ cm, as shown in Fig. 5(a). When the particle loading is increased to $400\,\mathrm{g/m^3}$ while keeping the same particle diameter, the mean cell width remains comparable, but the cellular structure becomes noticeably more irregular. Pronounced peak-pressure amplification occurs near the cellular vertices, indicating enhanced detonation instability [50]. This behavior is also reflected in Fig. 6, where increasing the particle loading from 50 to $400\,\mathrm{g/m^3}$ leads to larger oscillation amplitudes in both the detonation speed and the leading-shock pressure. To assess the influence of the transverse domain size on the cellular structure, additional

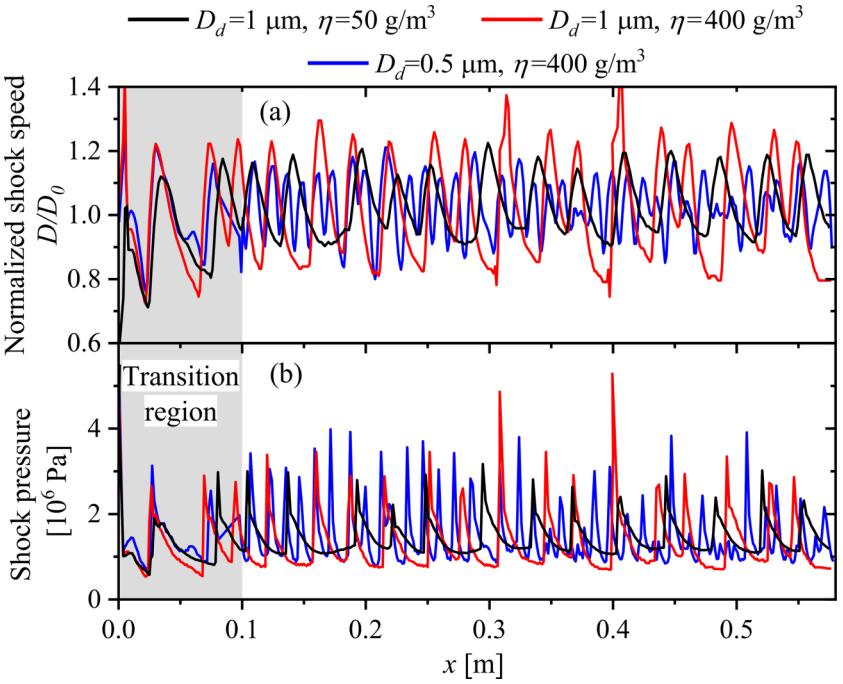


FIG. 6. Evolution of (a) normalized detonation speed D/D_0 and (b) shock pressure along the centerline ($y = 0$) for the cases in Fig. 5.

simulations were performed for Cases A and B, with the domain width increased from 5 to 10 cm. The resulting characteristic cell size and overall cellular pattern remain essentially unchanged, indicating that the adopted 5 cm transverse width is sufficient for the present simulations. Further details are provided in Sec. D of the Supplemental Material [29].

As shown in Fig. 5(c), reducing the particle diameter to 0.5 μm at fixed $\eta_0 = 400\,\mathrm{g/m^3}$ significantly decreases the mean cell size to $\lambda \approx 0.6$ cm. This reduction is attributed to the larger specific surface area and faster heating rate of smaller particles, which shorten the particle ignition delay and the associated induction length [6]. The resulting stronger gas–particle coupling increases the frequency of transverse-wave interactions, thereby reducing the detonation cell size [51]. Consistently, Fig. 6 shows that smaller particles increase the oscillation frequency of the centerline shock speed while reducing its oscillation amplitude, suggesting a dynamically more stable detonation front characterized by more frequent but weaker shock–reaction coupling cycles.

Figure 7 summarizes the variation of detonation cell size with the particle diameter for Al/air and Al/O_2 mixtures, together with data from previous studies and the present simulations. Over the particle-diameter range of 0.1 to 10 μm, the cell size of Al-particle detonations increases with particle diameter. Fedorov and Khmel [52] further proposed a power-law correlation between the cell size and particle diameter, i.e.,

$$\lambda = \lambda_0 (D_d / D_{d,0})^n, \tag{2}$$

where λ_0 and $D_{d,0}$ denote the reference cell size and particle diameter, respectively. Here, $\lambda_0 = 10$ mm and $D_{d,0} = 1$ μm are adopted, as several Al-particle detonation studies report a cell size of approximately 10 mm for 1 μm particles [52,55]. Based on the compiled data, the best-fit exponent is $n = 1.42$, as shown by the dashed line in Fig. 7. Overall, the present results are consistent with the empirical particle-size trend suggested by the compiled literature data, showing that larger Al particles generally lead to larger detonation cell sizes for similar Al–oxidizer detonation systems.

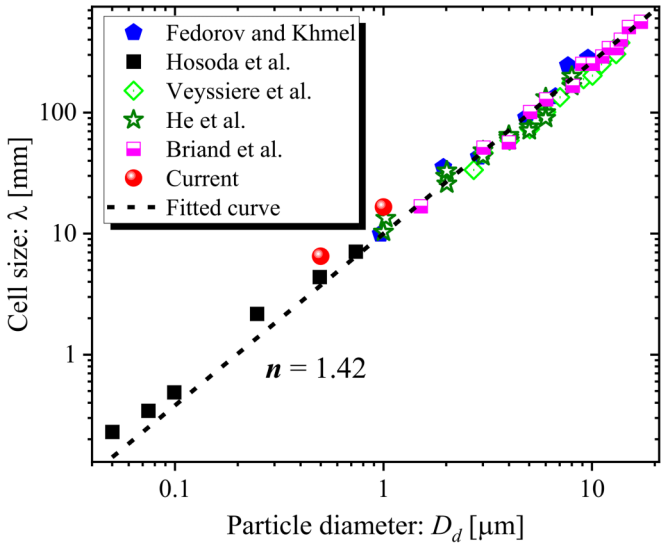


FIG. 7. Detonation cell size as a function of particle diameter for aluminum/air and aluminum/oxygen mixtures. Literature data are taken from Fedorov and Khmel [52], Hosoda *et al*. [53], Veyssiere *et al*. [16], He *et al*. [6], and Briand *et al*. [54].

Figure 8 presents the trajectories of peak pressure, peak heat release rate ($\dot{q}_{\mathrm{HRR,max}}$), and the corresponding particle volume fraction ($\alpha_{d,\mathrm{max}}$) for three cases in Fig. 6. The peak-pressure trajectories closely follow those of the peak HRR, indicating a strong correlation between pressure amplification and localized particle heat release. However, distinct heat-release characteristics are observed under fuel-lean and fuel-rich conditions.

For the low-loading case ($\eta_0 = 50\,\mathrm{g/m^3}$), a pronounced peak-HRR tail appears immediately downstream of the cell vertex, as shown in the middle panel of Fig. 8(a). Under fuel-lean conditions, oxygen is abundant; therefore, locally increased particle concentration, represented by the high-volume-fraction particle tail in the bottom panel of Fig. 8(a), promotes surface reactions and enhances heat release. In addition, relatively high particle concentrations are observed along the triple-point trajectories, leading to elevated local HRR maxima and well-defined heat-release cellular patterns.

In contrast, for the high-loading cases ($\eta_0 = 400\,\mathrm{g/m^3}$), the local particle volume fraction reaches a minimum along the triple-point trajectories, where the peak HRR attains its maximum. Appreciable heat release is also observed in the downstream half of the cell structures, as shown in the middle panels of Figs. 8(b) and 8(c). The particle-clustering tails correspond to extremely fuel-rich conditions ($\alpha_d \approx 0.3\%$, $\Phi \approx 54$), under which the heat supplied by the local hot gases is insufficient to trigger rapid surface oxidation. These observations indicate that the particle-concentration-controlled surface-reaction behavior in fuel-rich mixtures is fundamentally different from that under fuel-lean conditions. A more detailed analysis of these distinct heat-release characteristics and their role in shaping the detonation frontal structures is provided in Sec. III A 2.

Additional cases with particle loadings of $\eta_0 = 100$, 150, and $250\,\mathrm{g/m^3}$ ($\Phi = 0.67$, 1.0, and 1.67, respectively) are further examined to assess whether the observed trends remain applicable under more moderate conditions. These cases show a progressive transition in both the heat-release distribution and wave-strength characteristics as the particle loading increases, bridging the behaviors observed in the original fuel-lean and fuel-rich cases. The corresponding results and discussion are provided in Sec. E of the Supplemental Material [29].

Figure 9 shows the temporal evolution of the particle volume fraction, with the cellular trajectories marked by blue dashed lines. In the detonation cell ABCD, two transverse waves (TWs) collide

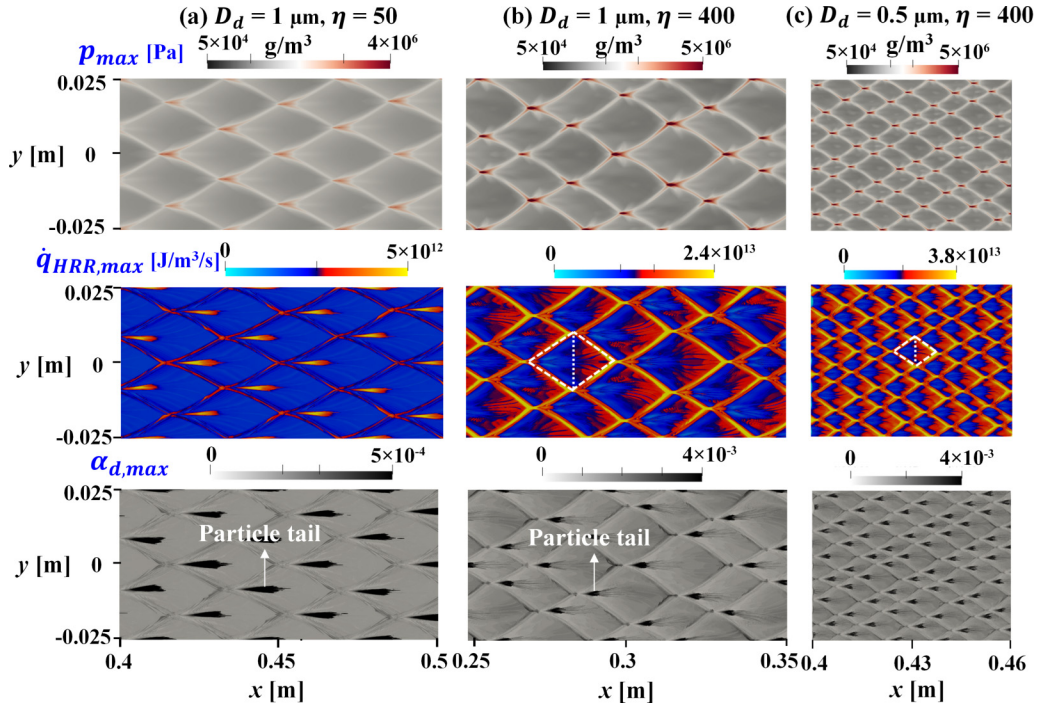


FIG. 8. Contours of peak pressure history ($p_{\max}$, top), peak heat release rate ($\dot{q}_{HRR,\max}$, middle), and particle volume fraction at the instant of peak HRR ($\alpha_{d,\max}$, bottom).

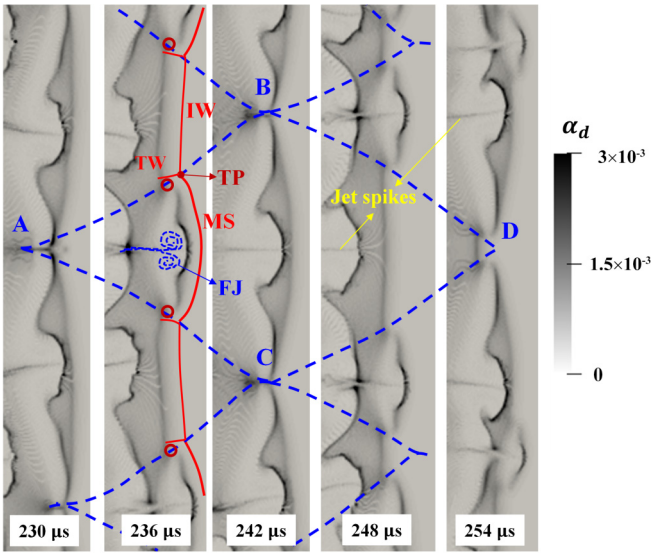


FIG. 9. Temporal evolution of particle-volume-fraction contours for $D_d = 1.0\,\mu\text{m}$ and $\eta_0 = 400\,\text{g/m}^3$. The red solid line denotes the leading shock front and the blue dashed lines indicate the cellular structure. TP: triple point; MS: Mach stem; IW: incident wave; TW: transverse wave; FJ: forward jet.

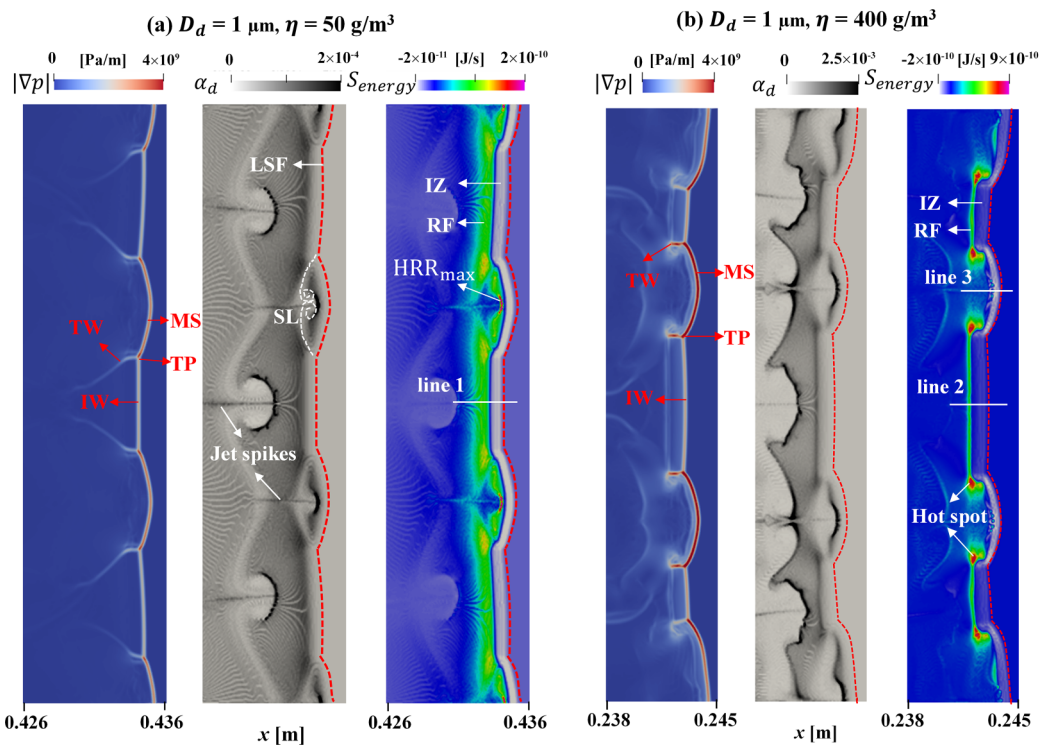


FIG. 10. Contours of pressure-gradient magnitude, particle volume fraction, and energy source term: (a) $\eta_0 = 50\,\mathrm{g/m^3}$ and (b) $\eta_0 = 400\,\mathrm{g/m^3}$. Particle diameter is $D_d = 1$ μm. MS: Mach stem; IW: incident wave; TW: transverse wave; TP: triple point; LSF: leading shock front; SL: shear layer; RF: reaction front; IZ: induction zone; HS: hot spot. Red dashed lines indicate the leading shock fronts.

at point A at 230 μs. The collision produces a localized hot spot with intense heat release, which drives the subsequent separation of the TWs from the cell vertex. At 236 μs, a forward jet (FJ) forms from point A and generates a Mach stem (MS) propagating at a velocity close to $1.4D_{\mathrm{CJ}}$. The combined action of the MS and FJ causes strong particle accumulation behind the MS, giving rise to the particle-clustering tail observed in Fig. 8. In addition, jet spikes develop along the trailing trajectory adjacent to the FJ, near the AD line. These spikes are relatively regular at low particle loadings but become increasingly unstable as the loading increases [6].

2. Coupling between cellular structures and particle energy release

Figure 10 presents contours of the pressure-gradient magnitude, particle volume fraction, and energy source term for the fuel-lean ($\eta_0 = 50\,\mathrm{g/m^3}$) and fuel-rich ($\eta_0 = 400\,\mathrm{g/m^3}$) cases. Figures 11(a) and 11(b) further show the normalized pressure-gradient magnitudes $|\nabla p|/|\nabla p|_{\max}$ in the vicinity of two representative triple points (TPs) in Figs. 10(a) and 10(b), respectively. Here, $|\nabla p|_{\max}$ is taken as the pressure-gradient magnitude associated with the Mach stem.

Under the fuel-lean condition in Fig. 10(a), the detonation frontal structure closely resembles that of a typical gaseous detonation, characterized by relatively weak but elongated transverse waves. As shown in Fig. 11(a), the Mach stem (MS) exhibits the largest pressure-gradient magnitude near the triple point and is therefore used as the reference level (100%). The incident wave (IW) reaches approximately 63% of this value, whereas the transverse wave (TW) is considerably weaker, at approximately 38%. Because the MS propagates at a velocity approaching $1.4D_{\mathrm{CJ}}$, it imposes the strongest compressive effect on the particles, leading to pronounced particle accumulation

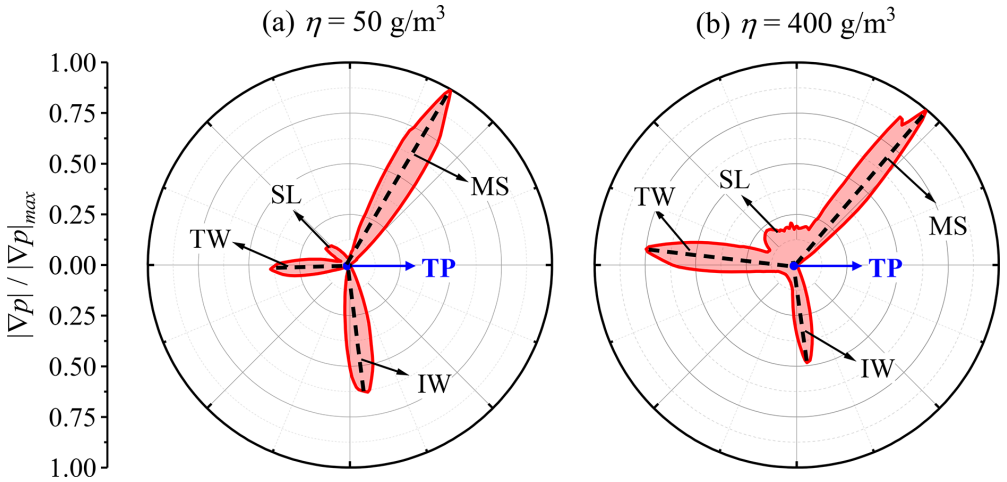


FIG. 11. Normalized pressure-gradient magnitude around representative triple points under fuel-lean and fuel-rich conditions. MS: Mach stem, IW: incident wave, TW: transverse wave, SL: shear layer.

downstream of the MS. This accumulation produces localized maxima in the heat release rate (HRR_{max}) and explains the peak-HRR tail observed in Fig. 8(a). The shear layer (SL), during vortex roll-up, promotes particle dispersion and generates a locally dilute region along its trajectory [15]. Coupled with the forward jet (FJ), this process leads to the formation of characteristic jet spikes [6]. Within the induction zone (IZ), identified by the white region behind the leading shock, S_{energy} is negative behind both the MS and IW, indicating comparable gas-to-particle heat transfer in these regions. The subsequent particle reaction fronts downstream of both waves are also spatially uniform. These features indicate a relatively stable detonative structure under fuel-lean conditions.

Under the fuel-rich condition in Fig. 10(b), one pronounced change is the shortening of the transverse wave, which becomes highly localized and hence is largely confined within the particle induction zone. However, the TW pressure gradient increases markedly (∼75%), exceeding that of the IW (∼50%), as shown in Fig. 11(b). The particles behind the TP are expected to experience more rapid heating than those in other regions, because they are first exposed to the high-temperature gas behind the Mach stem and may subsequently undergo additional compressive heating associated with the transverse wave. Consequently, these particles ignite and react rapidly, forming an intense energy release region along the TP trajectory, identified as the hot spot in Fig. 10(b). This rapid and localized heat release effectively energizes the TW, producing a high-pressure spot that promotes its lateral propagation.

In contrast to the fuel-lean case, although the MS induces the strongest compression, the region behind it exhibits relatively weak surface-reaction heat release, while convective heat transfer dominates within the induction zone. This behavior is primarily associated with the pronounced particle accumulation behind the MS, which enhances interphase heat absorption. In comparison, particle accumulation behind the relatively weaker IW is less pronounced, providing a more favorable oxidizer environment and allowing stronger surface reactions to develop. A more detailed comparison of the post-IW and post-MS regions is provided in Sec. F of the Supplemental Material [29].

Figure 12 further compares the distributions of particle volume fraction (α_d), energy source term (S_{energy}), and oxygen concentration (ρ_{O2}) along the three representative lines shown in Fig. 10. For the fuel-lean case, line 1 crosses the incident wave. Immediately behind the IW, S_{energy} becomes negative within the induction zone, indicating convective heat transfer from the gas phase to the particles. After this heating stage, the particles ignite, and surface reactions are initiated, forming the reaction zone. The reaction region is relatively broad, with a thickness of approximately 2.4

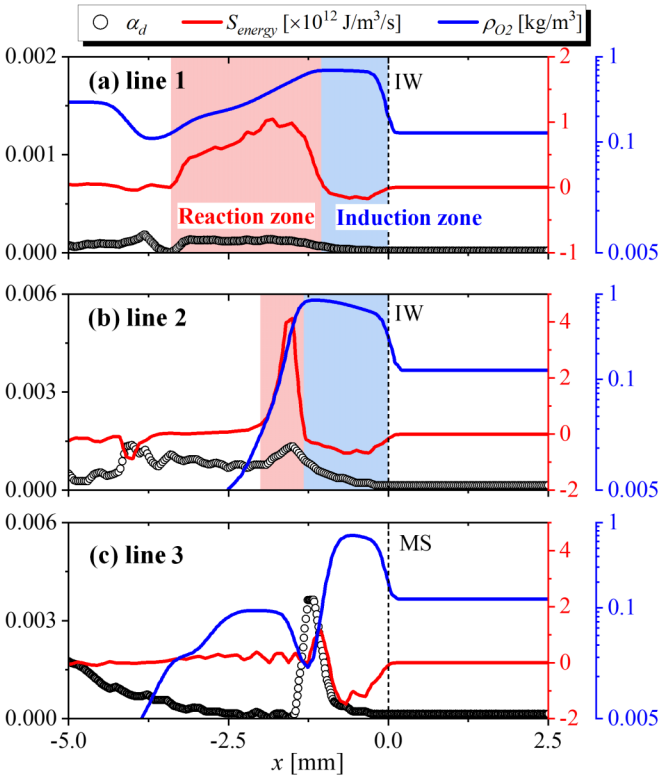


FIG. 12. Distributions of particle volume fraction α_d, energy source term S_{energy} and oxygen concentration ρ_{O2} along the three lines marked in Fig. 10.

mm, and the peak heat-release rate reaches $1.04 \times 10^{12}\,\text{J/m}^3/\text{s}$. Downstream of the reaction zone, the particles are largely consumed, while a substantial amount of oxygen remains, consistent with the fuel-lean condition.

For the fuel-rich case, line 2 also crosses the IW structure but exhibits a much more localized and intense reaction. The peak heat-release rate increases to $4.11 \times 10^{12}\,\text{J/m}^3/\text{s}$, whereas the reaction-zone thickness decreases to about 0.6 mm. This indicates that higher particle loading enhances the local surface-reaction intensity but confines the heat release to a much thinner region. A different behavior is observed along line 3, which crosses the Mach stem. In this region, strong particle accumulation occurs behind the MS, with the peak particle volume fraction reaching approximately 0.4%. The excessive particle concentration leads to strong post-MS heat absorption, which suppresses the particle-temperature rise and delays particle ignition. Consequently, the peak heat-release rate ($1.15 \times 10^{12}\,\text{J/m}^3/\text{s}$) is even lower than the maximum endothermic rate ($1.46 \times 10^{12}\,\text{J/m}^3/\text{s}$). Downstream of the MS, oxygen is consumed only gradually through weak residual reactions, accompanied by low-amplitude oscillations in the heat-release rate.

Figure 13 provides a schematic of the detonation-front structure and associated energy-release profiles under fuel-lean and fuel-rich conditions. The relative strengths of different wave components are indicated by the line thickness. For the fuel-lean case shown in Fig. 13(a), the wave-strength hierarchy near the triple point follows MS > IW > TW. In the postshock region, both the induction zone (IZ, blue region) and the reaction zone (RZ, red region) are distributed almost uniformly behind the leading shock, resembling the characteristic structure of gaseous detonations.

In contrast, the fuel-rich case shown in Fig. 13(b) exhibits a different wave-strength ordering near the TP, namely, MS > TW > IW. Both interphase convective heat transfer (blue) and

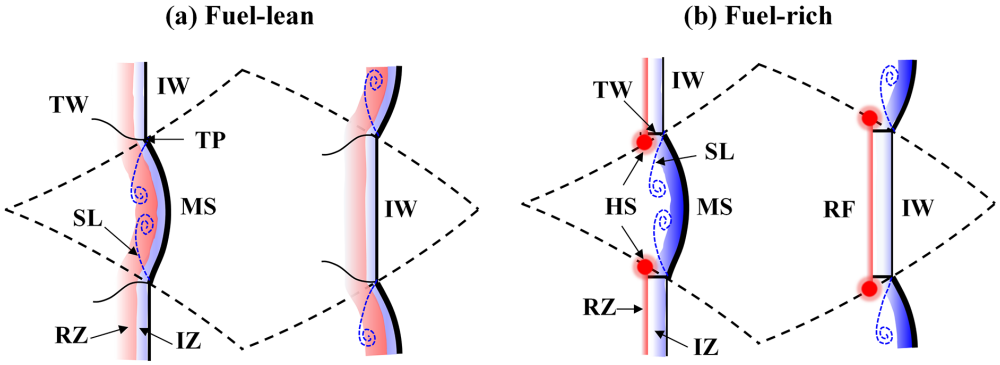


FIG. 13. Schematic illustration of the cellular front structures under fuel-lean and fuel-rich conditions. The red region denotes the reaction zone, whereas the blue region represents the induction zone. The color intensity qualitatively indicates the magnitude of the local energy release. Abbreviations are consistent with those in Fig. 10.

surface-reaction heat release (red) behind the leading shock exhibit highly nonuniform spatial distributions. Specifically, interphase convective heat transfer is the strongest behind the MS, whereas surface-reaction heat release behind the MS is much weaker than that behind the IW. A pronounced hot spot forms behind the TP and migrates along the cellular trajectory. The hot spot along the TP trajectory constitutes the dominant pathway for reaction-energy release, followed by appreciable surface reactions downstream of the IW. By contrast, the MS region contributes negligibly to surface-reaction heat release because excessive particle loading absorbs substantial heat and suppresses ignition, as detailed in Fig. 12.

B. Nonuniform particle loading

1. Wavelength-controlled cellular modulation and localized reinitiation

This section examines the influence of nonuniform particle loading on heterogeneous detonation dynamics. Figure 14 presents the peak-pressure trajectories with different loading wavelengths.

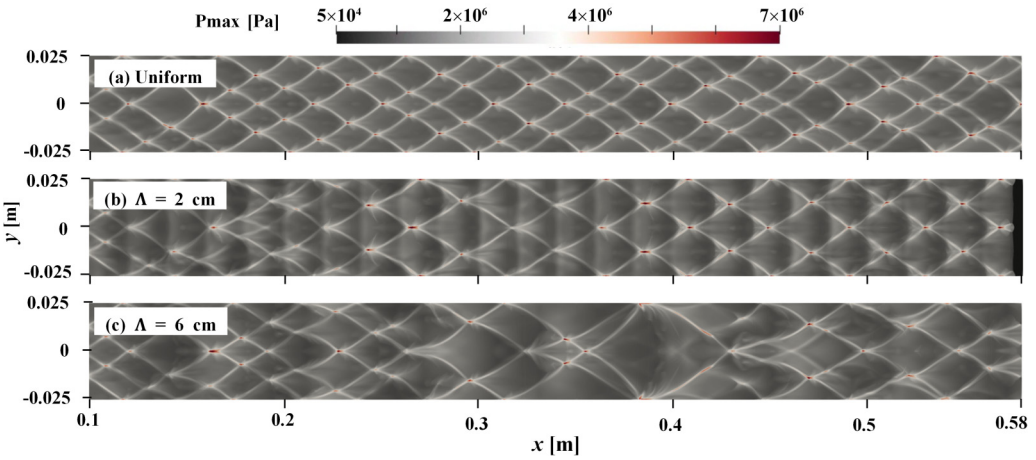


FIG. 14. Trajectories of peak pressure with different loading wavelengths. The reference uniform particle loading is $\eta_0 = 400\,\mathrm{g/m^3}$, and the particle diameter is $D_d = 1\,\mu\mathrm{m}$.

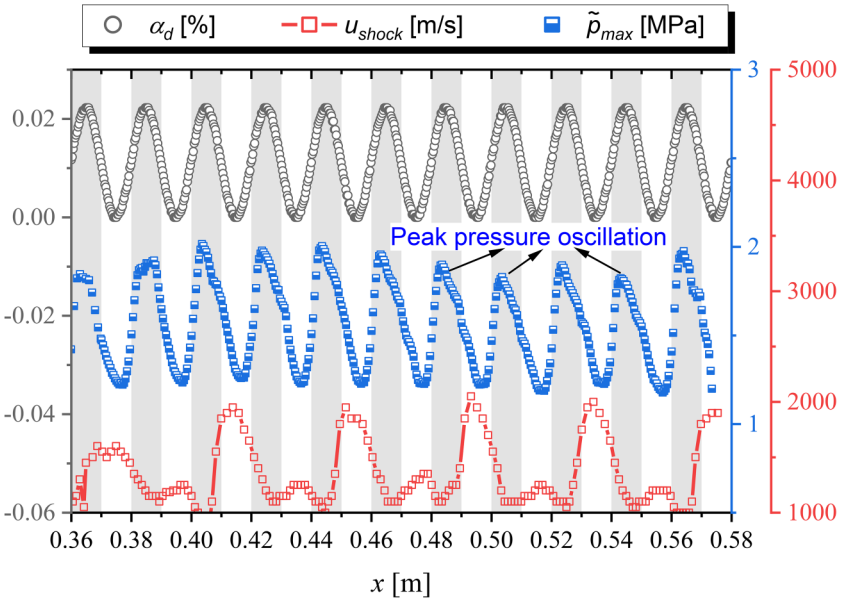


FIG. 15. Distributions of the particle-loading profile, centerline detonation speed ($y = 0$), and Favre-averaged peak pressure for the case $\Lambda = 2$ cm. The gray and white regions denote the high- and low-loading regions, respectively.

The mean loading is $\eta_0 = 400\,\mathrm{g/m^3}$. The uniform-loading case exhibits relatively regular cellular structures with the smallest cell size ($\lambda \approx 1.7$ cm). When a finite loading wavelength is introduced, the cellular structure becomes increasingly modulated by the imposed particle loading variation. In the nonuniform cases, a periodic modulation of the peak pressure is superimposed on the intrinsic cellular pattern, and this modulation follows the imposed loading wavelength. This peak-pressure modulation is further quantified and discussed in Fig. 15. For $\Lambda = 2$ cm, the detonation front still maintains a relatively regular cellular structure, although local distortions and enlarged cell spacing become evident ($\lambda \approx 2.5$ cm). As the loading wavelength increases to $\Lambda = 6$ cm, the cellular pattern becomes more irregular, with enlarged and distorted cells and stronger spatial variations in peak pressure. These results indicate that the imposed loading wavelength significantly affects transverse-wave dynamics and the regularity of the detonation cellular structure.

Figure 15 shows the distributions of particle loading, centerline detonation speed ($y = 0$), and Favre-averaged peak pressure ($\tilde{P}_{\max}$) when $\Lambda = 2$ cm. $\tilde{P}_{\max}$ is calculated as

$$\tilde{P}_{\max} = \frac{\sum_{y,i} p_{\max} \rho_i V_i}{\sum_{y,i} \rho_i V_i}, \tag{3}$$

where i denotes the i-th CFD cell along the y direction. Notably, the oscillation of $\tilde{P}_{\max}$ is almost in phase with the imposed loading profile: high-loading (low-loading) regions correspond to high-pressure (low-pressure) regions. Similar peak-pressure oscillations were reported by Xi *et al.* [21] for gaseous cellular detonations in hydrogen/air mixtures with sinusoidal density distributions, and this propagation behavior was referred to as mode locking [56]. The present detonation, however, exhibits a different coupling between peak pressure and shock speed. Specifically, strong interphase drag in the particle induction zone can cause the peak pressure location to persistently lag behind the leading shock, while maintaining a pressure level higher than the shock pressure [49]. Consequently, in high-loading regions, the stronger drag and delayed particle heat release prevent the localized pressure amplification from immediately feeding back to the leading shock. These regions therefore

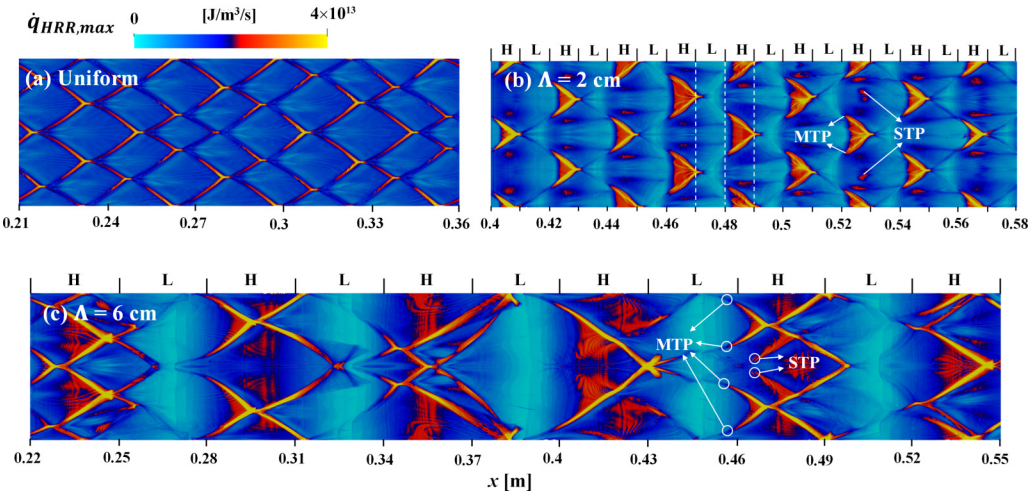


FIG. 16. Trajectories of peak heat release rate ($\dot{q}_{HRR,\max}$) for cases with different particle-loading wavelengths. Symbols denote regions of high (H) and low (L) particle loading, respectively. MTP: main triple point, STP: secondary triple point.

correspond to local minima in shock speed, as shown in Fig. 15. In contrast, the shock-speed maxima generally occur in the low-loading regions, where the drag effect is weaker and the leading shock experiences weaker drag-induced attenuation. A more detailed comparison of the pressure and heat release characteristics in the high- and low-loading regions is provided in Sec. G of the Supplemental Material [29].

To further clarify the influence of particle-loading modulation on the local energy-release process, Fig. 16 presents the trajectories of peak heat release rate for selected regions in Fig. 14. For the uniform loading case, significant heat release is mainly concentrated along regular triple point trajectories. When longitudinal particle-loading variation is introduced, the heat release distribution becomes strongly affected by the alternating high- and low-loading regions. For $\Lambda = 2$ cm, the particle heat release is dominant in the high-loading (H) regions, particularly along the main triple point (MTP) trajectory and the connecting region swept by the incident wave. In contrast, the heat release intensity is substantially reduced in the low-loading (L) regions. As a result, when the leading shock propagates through a low-loading region, its behavior becomes increasingly shock-dominated, with a tendency for the reaction front to decouple from the shock front [20]. In addition, secondary triple points (STP) occasionally emerge in the high-loading regions, although their heat release intensity is much weaker than that associated with the MTP.

For $\Lambda = 6$ cm, the heat release field becomes highly intermittent and spatially inhomogeneous. Strong heat release spots are still concentrated along the MTP trajectories, but the intensity and spatial extent of the heat release associated with the STPs also increase markedly. Meanwhile, the energy release pathways become partially interrupted, leading to a more irregular cellular structure. In particular, the marked MTP and STP locations in Fig. 16(c) correspond to local reinitiation events, where intensified particle heat release promotes the recovery of a coupled shock–reaction structure. The temporal evolution of these reinitiation processes will be further examined in Fig. 17.

Figure 17 presents the temporal evolution of the pressure gradient magnitude, gas temperature, and oxygen mass fraction for the case with $\Lambda = 6$ cm. At $t = 350\,\mu$s, a distorted leading shock is observed, with several transverse waves (TW1–TW4) generated behind the front. Unreacted pockets appear downstream of the leading shock, characterized by relatively low temperature and residual oxygen. At $t = 354\,\mu$s, several reinitiation (RI) sites emerge near the MTPs, accompanied by localized gas heating and oxygen consumption close to the shock front.

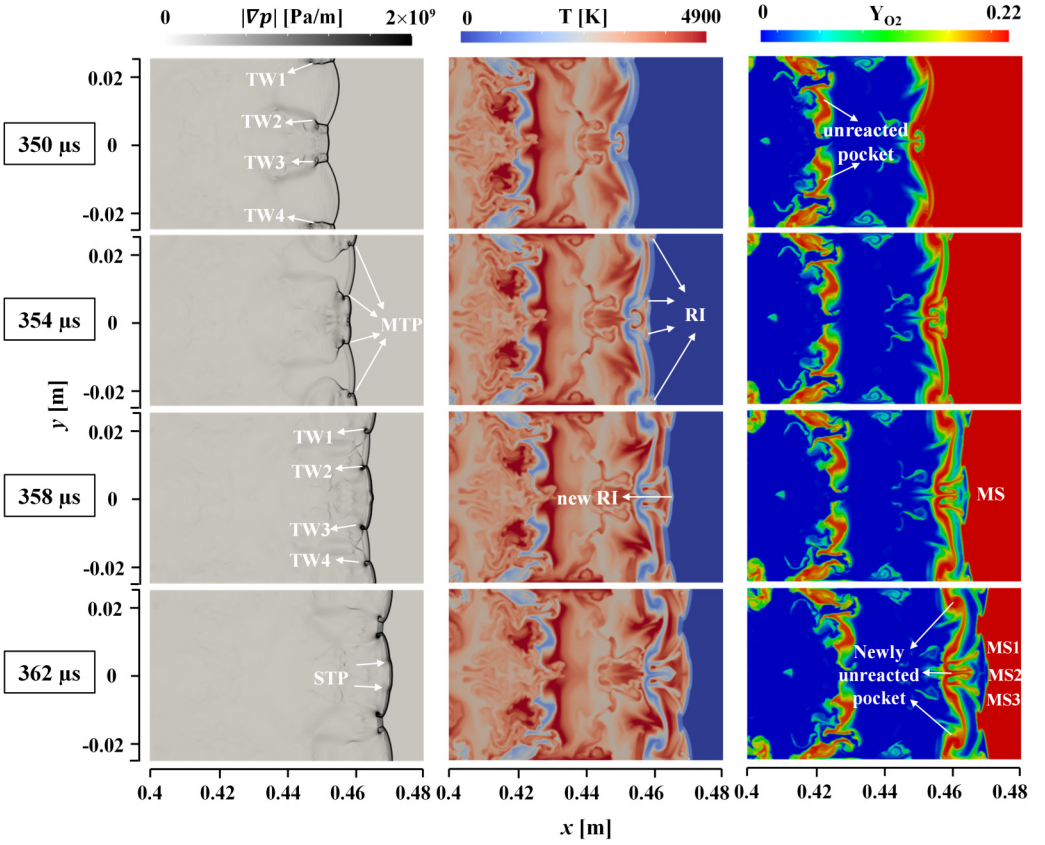


FIG. 17. Evolution of gas temperature, oxygen mass fraction, and pressure-gradient magnitude at different time instants for the wavelength $\Lambda = 6$ cm. TW: transverse wave, MTP: main triple point, STP: secondary triple point, MS: Mach stem, and RI: reinitiation site.

As the process develops to $t = 358\,\mu$s, the detonation front propagates from a low-loading region ($0.43 < x < 0.46$ m) into a high-loading region ($0.46 < x < 0.49$ m). During this transition, the transverse waves become shorter and stronger, consistent with the transition from fuel-lean-like to fuel-rich-like frontal structures summarized schematically in Fig. 13. Subsequently, a diverging detonation structure forms, characterized by a curved Mach stem that propagates laterally and enhances the local shock compression. This process promotes a new RI event along the Mach stem, where the locally enhanced reactivity causes wrinkling of the leading front [57].

At $t = 362\,\mu$s, the newly formed RI propagates forward with a relatively high local velocity, leading to the formation of secondary triple points. Although these STPs are weaker than the MTP, they modify the local wave configuration and split the original parent Mach stem into three child Mach stems, denoted as MS1–MS3. Meanwhile, the reaction front generated by the RI sites in the high-loading region recouples with the leading shock. This interaction reshapes the front and leaves a newly formed unreacted pocket behind the distorted leading shock. Overall, Fig. 17 shows that the large-wavelength loading modulation promotes intermittent shock–reaction decoupling and localized reinitiation, which are responsible for the irregular cellular structures observed in Fig. 16.

2. Particle-size effects on shock–reaction coupling under modulated loading

To further assess the role of particle response time under modulated loading, Figs. 18 and 19 present the corresponding peak-pressure and peak-HRR trajectories for $D_d = 0.5\,\mu$m at the mean

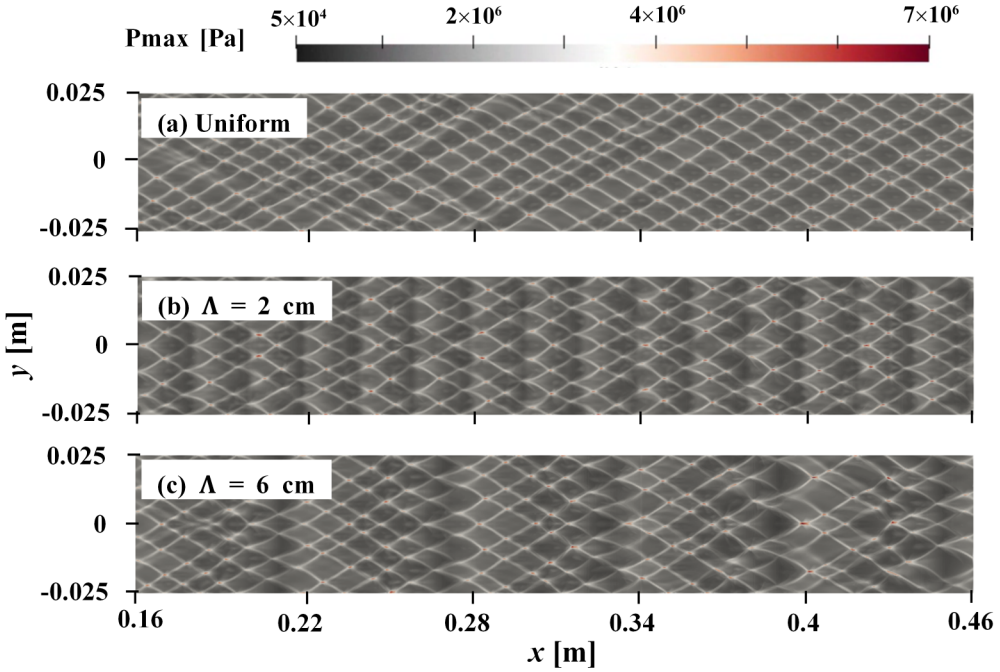


FIG. 18. Trajectories of peak pressure for cases with different loading wavelengths. The reference uniform particle loading is $\eta_0 = 400\,\mathrm{g/m^3}$, and the particle diameter is $D_d = 0.5\,\mu\mathrm{m}$.

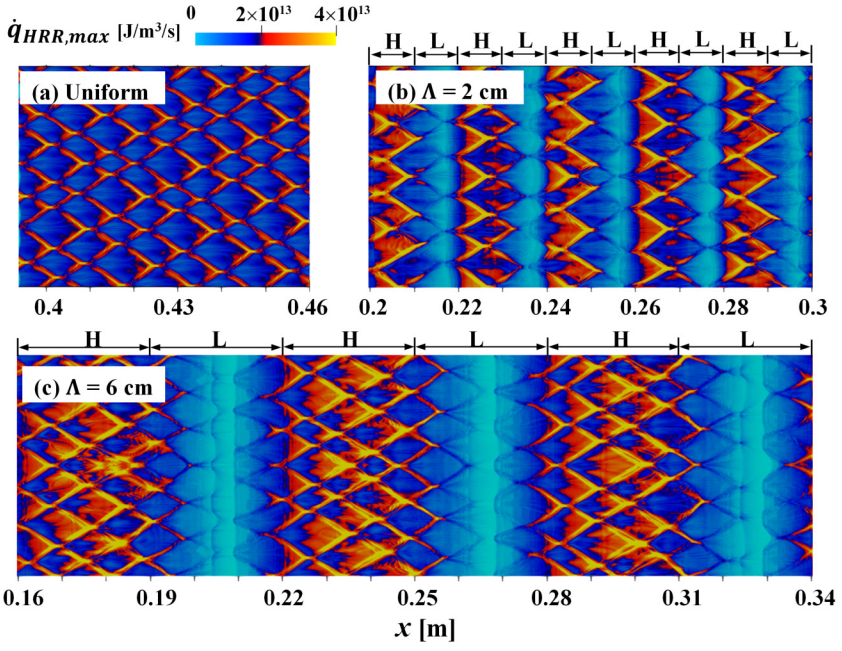


FIG. 19. Trajectories of peak heat release rate ($\dot{q}_{HRR,\max}$) for cases with different particle-loading wavelengths. Symbols denote regions of high (H) and low (L) particle loading, respectively.

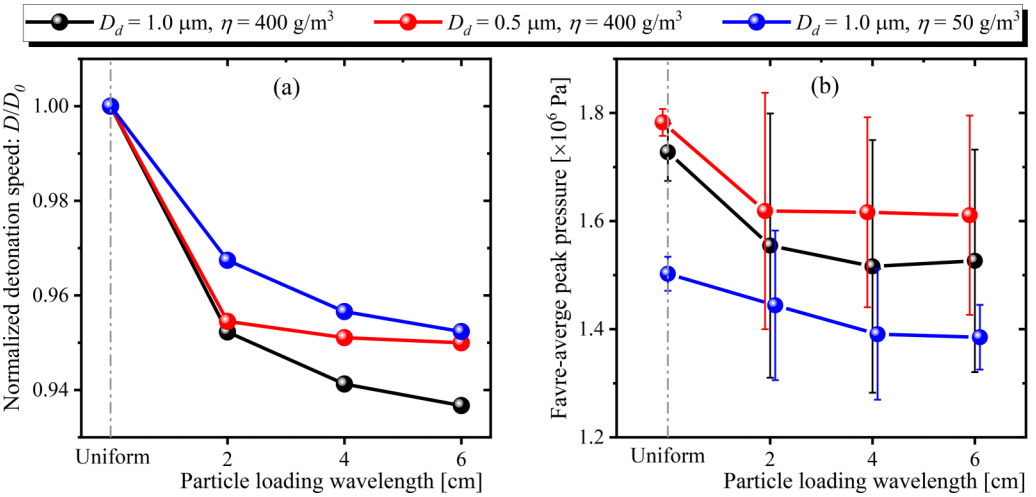


FIG. 20. Evolution of (a) normalized detonation speed and (b) Favre-averaged peak pressure with different particle loading wavelengths. The error bars in panel (b) represent the RMS amplitudes of the peak-pressure oscillations.

loading of $\eta_0 = 400\,\mathrm{g/m^3}$. As shown in Fig. 18, when longitudinal particle-loading modulation is introduced, the imposed high- and low-loading regions still affect the peak pressure trajectories, but the cellular network remains more continuous than that observed for $D_d = 1\,\mu\mathrm{m}$ in Fig. 14. For $\Lambda = 2$ cm, several small cells are contained within each loading period, and the modulation mainly appears as a periodic variation in local pressure intensity rather than a complete disruption of the cellular structure. As the loading wavelength increases to $\Lambda = 6$ cm, the peak-pressure field becomes more spatially modulated, with locally enlarged and distorted cells in the low-loading regions. Nevertheless, the overall cellular pattern remains finer and less severely disrupted than in the corresponding $D_d = 1\,\mu\mathrm{m}$ case.

Figure 19 further shows the trajectories of the peak heat release rate for the same set of cases. In the uniform-loading case, intense heat release is concentrated along closely spaced triple-point trajectories, forming a regular fine-scale cellular pattern. Under nonuniform loading conditions, the particle heat release is preferentially enhanced in the high-loading regions and weakened in the low-loading regions, consistent with the behavior observed for $D_d = 1\,\mu\mathrm{m}$. However, because smaller particles ignite more rapidly, the HRR traces remain more continuous across the modulated field. Even for $\Lambda = 6$ cm, where the separation between high- and low-loading regions is most evident, the low-loading regions still retain discernible reaction traces instead of exhibiting complete shock–reaction decoupling. These results indicate that reducing the particle diameter mitigates the destabilizing effect of particle-loading modulation by promoting faster energy release and more robust shock–reaction coupling.

Figure 20 summarizes the effects of particle-loading wavelength on the normalized detonation speed and Favre-averaged peak pressure. The supplemental results in Sec. H of the Supplemental Material [29] further examine the case with $D_d = 1\,\mu\mathrm{m}$ and $\eta_0 = 50\,\mathrm{g/m^3}$, showing that the low-loading (fuel-lean) condition is more resistant to loading-induced perturbations. As shown in Fig. 20(a), introducing longitudinal particle-loading modulation leads to a reduction in the mean detonation speed for all cases. This speed deficit becomes more pronounced as the loading wavelength increases, indicating that longer-wavelength modulation more strongly disrupts the global shock–reaction coupling. Among the high-loading cases ($\eta_0 = 400\,\mathrm{g/m^3}$), the larger particles ($D_d = 1\,\mu\mathrm{m}$) exhibit the greatest reduction in propagation speed, whereas the smaller particles ($D_d = 0.5\,\mu\mathrm{m}$) partly mitigate this loss. This is consistent with the shorter ignition delay and faster

energy release of smaller particles, which enhance the ability of the detonation front to withstand loading-induced disturbances. The low-loading case ($\eta_0 = 50\,\mathrm{g/m^3}$) shows a smaller speed deficit than the corresponding high-loading case with the same particle diameter ($D_d = 1\,\mu\mathrm{m}$). Additional analysis indicates that its mean cell size is only weakly affected by the loading wavelength, although the cellular regularity decreases as the wavelength increases. This suggests that, under fuel-lean conditions, longitudinal loading modulation mainly perturbs the regularity of the cellular pattern rather than causing strong degradation of the mean propagation speed.

Figure 20(b) shows that the Favre-averaged peak pressure is also sensitive to the loading wavelength. The high-loading cases exhibit higher mean peak pressures than the low-loading case because of stronger local compression and more intense particle heat release. Under modulated-loading conditions, the enlarged error bars indicate stronger peak-pressure oscillations and enhanced detonation unsteadiness. In particular, the high-loading case with larger particles produces larger pressure fluctuations, reflecting stronger intermittent shock–reaction decoupling and delayed energy release. Overall, larger particle size and higher particle loading amplify the destabilizing effect of longitudinal loading modulation, leading to a larger propagation-speed deficit and stronger peak-pressure fluctuations.

IV. CONCLUSION

In this study, the propagation characteristics and cellular structures of aluminum–air heterogeneous detonations are systematically investigated, with emphasis on the effects of off-stoichiometric particle loading, particle size, and longitudinal loading nonuniformity. A two-way coupled Eulerian–Lagrangian numerical framework is employed to resolve gas–particle mass, momentum, and energy exchange. The predicted detonation velocities agree reasonably well with theoretical and experimental data, indicating that the present model is capable of capturing the main propagation features of aluminum-particle detonations.

For uniform particle distributions, increasing the particle loading enhances the irregularity of the cellular structure and strengthens the oscillations of detonation speed and shock pressure, indicating reduced detonation stability. Decreasing the particle diameter markedly reduces the cell size and weakens the oscillation amplitude, owing to faster particle heating, shorter ignition delay, and stronger gas–particle coupling. Detailed analysis reveals distinct energy-release pathways under fuel-lean and fuel-rich conditions. In the fuel-lean case, the postshock structure resembles that of gaseous detonations, with relatively uniform induction and reaction zones and a wave-strength hierarchy of MS > IW > TW. In the fuel-rich case, this hierarchy changes to MS > TW > IW. Intense localized heat release develops behind the transverse wave and along the triple-point trajectory, whereas excessive particle accumulation behind the Mach stem suppresses surface reactions through strong convective heat absorption. Consequently, the hot spot along the triple-point path becomes the dominant heat release pathway, producing strong spatial inhomogeneity and reduced stability.

For nonuniform particle distributions, increasing the loading wavelength enlarges the cell size, distorts the cellular pattern, and promotes intermittent shock–reaction decoupling and local reinitiation, especially under fuel-rich conditions. The Favre-averaged peak pressure exhibits a large-scale modulation that follows the imposed loading profile, although longer wavelengths lead to phase shifts and reduced coherence. High local heat release does not necessarily strengthen the leading shock, because particle-induced momentum loss can delay and weaken the feedback of pressure amplification to the shock front. Smaller particles and fuel-lean loadings show stronger resistance to loading-induced perturbations.

Overall, the results demonstrate that the stability of Al–air heterogeneous detonations is jointly controlled by particle loading, particle diameter, and the wavelength of loading modulation through their effects on particle response, interphase transport, and localized surface-reaction pathways.

ACKNOWLEDGMENTS

This work was supported by National Key Laboratory of Shock Wave and Detonation Physics Open Fund (No. 2025JCJQLB10403). The computations in this study were partially performed using the Sugon high-performance computing system. P.Z. acknowledges Dr. Qingyang Meng at The Hong Kong Polytechnic University for valuable discussions.

DATA AVAILABILITY

There are no publicly available research data or software supporting this manuscript. Requests for further information or data should be sent to the authors.

[1] T. Han, Y. Xu, C. Jiao, and Y. Wang, Numerical study of initiation characteristics in aluminum/air rotating detonation engines, Acta Astronaut. **245**, 698 (2026).

[2] Z. Zhang, J. Jing, B. Meng, H. Ma, and Z. Xia, *Numerical Simulation of Gas-solid Two-phase Rotating Detonation Engine Based on Aluminum Powder Fuel. 2nd Asian Aerospace and Astronautics Conference*: (IEEE, 2024), pp. 133–141.

[3] M. V. Papalexandris, Numerical simulation of detonations in mixtures of gases and solid particles, J. Fluid Mech. **507**, 95 (2004).

[4] J. W. Posey, B. Roque, S. Guhathakurta, and R. W. Houim, Mechanisms of prompt and delayed ignition and combustion of explosively dispersed aluminum powder, Phys. Fluids **33**, 113308 (2021).

[5] Z. J. Zhang, C. Y. Wen, Y. F. Liu, D. L. Zhang, and Z. L. Jiang, Effects of different particle size distributions on aluminum particle–air detonation, AIAA J. **58**, 3115 (2020).

[6] J. He, B. Meng, B. Tian, H. Li, and J. Li, Numerical study of two-phase detonation in dilute aluminum particle-air mixtures using Eulerian-Lagrangian approach, Combust. Flame **275**, 114110 (2025).

[7] Q. Zhou, J. Huang, W. Han, and C. Wang, Initiation and propagation of one-dimensional detonations in aluminum-particle/C_2H_2/Air system, Phys. Fluids **34**, 102408 (2022).

[8] T. Khmel and S. Lavruk, Detonation flows in aluminium particle gas suspensions, inhomogeneous in concentrations, J. Loss Prev. Process Ind. **72**, 104522 (2021).

[9] F. Zhang, S. B. Murray, and K. B. Gerrard, Aluminum particles–air detonation at elevated pressures, Shock Waves **15**, 313 (2006).

[10] F. Zhang, H. Grönig, and A. Van de Ven, DDT and detonation waves in dust-air mixtures, Shock Waves **11**, 53 (2001).

[11] P. Zhang, Y. Xu, H. Zhang, and Z. Chen, Unsteady dynamics and mode transitions in hybrid hydrogen–aluminum detonations, Combust. Flame **281**, 114438 (2025).

[12] P. S. Kuleshov and V. D. Kobtsev, Distribution of aluminum clusters and their ignition in air during dispersion of aluminum nanoparticles in a shock wave, Combust. Explos. Shock Waves **56**, 566 (2020).

[13] F. Zhang, Detonation in reactive solid particle-gas flow, J. Propul. Power **22**, 1289 (2006).

[14] B. Veyssiere, Detonations in gas-particle mixtures, J. Propul. Power **22**, 1269 (2006).

[15] J. Zhang, S. Li, Q. Meng, S. Li, and H. Zhang, Detonative wavelets in quasi-detonations with fine coal char particles, Combust. Flame **275**, 114101 (2025).

[16] B. Veyssiere, B. A. Khasainov, and A. Briand, Investigation of detonation initiation in aluminium suspensions, Shock Waves **18**, 307 (2008).

[17] T. A. Khmel and S. A. Lavruk, Modeling of cellular detonation in gas suspensions of submicron aluminum particles with different distributions of concentration, Combust. Explos. Shock Waves **58**, 253 (2022).

[18] T. A. Khmel and S. A. Lavruk, Interaction of cellular detonation in aluminum particle suspensions with nonuniform concentrations and clouds of inert particles, Combust. Explos. Shock Waves **59**, 308 (2023).

[19] A. A. Afanasenkov and T. A. Khmel, Modeling of hybrid detonation in an inhomogeneous gas suspension of aluminum particles, Combust. Explos. Shock Waves **61**, 1014 (2026).

[20] Y. Wang, C. Huang, R. Deiterding, H. Chen, and Z. Chen, Numerical studies on detonation propagation in inhomogeneous mixtures with periodic reactant concentration gradient, J. Fluid Mech. **955**, A23 (2023).
[21] X. Xi, H. Teng, Z. Chen, and P. Yang, Effects of longitudinal disturbances on two-dimensional detonation waves, Phys. Rev. Fluids **7**, 043201 (2022).
[22] J. Fujii, Y. Kumazawa, A. Matsuo, S. Nakagami, K. Matsuoka, and J. Kasahara, Numerical investigation on detonation velocity in rotating detonation engine chamber, Proc. Combust. Inst. **36**, 2665 (2017).
[23] D. S. Sundaram, P. Puri, and V. Yang, A general theory of ignition and combustion of nano- and micron-sized aluminum particles, Combust. Flame **169**, 94 (2016).
[24] P. Zhang, H. Zhang, Y. F. Zhang, S. Li, and Q. Meng, Modeling particle collisions in moderately dense curtain impacted by an incident shock wave, Phys. Fluids **35**, 023327 (2023).
[25] P. Zhang and H. Zhang, Instabilities of a circular moderately dense particle cloud impacted by an incident shock, Int. J. Multiphase Flow **174**, 104787 (2024).
[26] D. M. Snider, An incompressible three-dimensional multiphase particle-in-cell model for dense particle flows, J. Comput. Phys. **170**, 523 (2001).
[27] J. Shi, P. Zhang, Y. Xu, W. Ren, and H. Zhang, Effects of dilute coal char particle suspensions on propagating methane detonation wave, Combust. Flame **249**, 112618 (2023).
[28] Y. Xu, P. Zhang, Q. Meng, S. Li, and H. Zhang, Transmission of hydrogen detonation across a curtain of dilute inert particles, Combust. Flame **254**, 112834 (2023).
[29] See Supplemental Material at http://link.aps.org/supplemental/10.1103/pxtc-m7bp for additional numerical methods, validation studies, and analyses of detonation structure and particle–gas interactions.
[30] E. Loth, J. T. Daspit, M. Jeong, T. Nagata, and T. Nonomura, Supersonic and hypersonic drag coefficients for a sphere, AIAA J. **59**, 3261 (2021).
[31] L. L. Kavanau, Heat transfer from spheres to a rarefied gas in subsonic flow, Trans. Am. Soc. Mech. Eng. **77**, 617 (1955).
[32] F. Zhang, K. Gerrard, and R. C. Ripley, Reaction mechanism of aluminum-particle-air detonation, J. Propul. Power **25**, 845 (2009).
[33] H. Teng and Z. Jiang, Numerical simulation of one-dimensional aluminum particle–air detonation with realistic heat capacities, Combust. Flame **160**, 463 (2013).
[34] S. Guhathakurta, *Propagation and Structure of Hybrid Aluminum-Hydrogen-Air Detonations: A Computational Approach, 30th ICDERS* (Ottawa, Canada, 2025).
[35] A. Kurganov, S. Noelle, and G. Petrova, Semidiscrete central-upwind schemes for hyperbolic conservation laws and Hamilton–Jacobi equations, SIAM J. Sci. Comput. **23**, 707 (2001).
[36] Z. Huang, M. Zhao, Y. Xu, G. Li, and H. Zhang, Eulerian-Lagrangian modelling of detonative combustion in two-phase gas-droplet mixtures with OpenFOAM: Validations and verifications, Fuel **286**, 119402 (2021).
[37] P. Zhang, C. Cao, and H. Zhang, Micron-sized aluminum particle combustion under elevated gas condition: Equivalence ratio effect, Appl. Energy Combust. Sci. **19**, 100283 (2024).
[38] P. Zhang, H. Zhang, and Y. F. Zhang, Kinetic studies of ignition of coal char particle suspension in hot air, Fuel **357**, 129977 (2024).
[39] J. Zhang, S. Li, P. Zhang, Q. Meng, and H. Zhang, Detonation initiation mode in non-uniform coal particle suspensions subject to an incident blast wave, Combust. Flame **288**, 114946 (2026).
[40] M. W. Beckstead, Correlating aluminum burning times, Combust. Explos. Shock Waves **41**, 533 (2005).
[41] J. Zhang, Z. Xia, L. Ma, O. T. Stein, Y. Feng, T. D. Luu, and A. Kronenburg, Sensitivity of flame structure and flame speed in numerical simulations of laminar aluminum dust counterflow flames, Combust. Flame **245**, 112363 (2022).
[42] A. A. Borisov, B. A. Khasainov, E. L. Saneev, I. B. Fomin, S. V. Khomik, and B. Veyssiere, On the detonation of aluminum suspensions in air and in oxygen, in *Dynamic Structure of Detonation in Gaseous and Dispersed Media*, edited by A. A. Borissov, Fluid Mechanics and Its Applications Vol. 5 (Springer, Dordrecht, 1991), pp. 215–253.
[43] R. D. Smith and S. B. Stanley, Experimental investigation of rotating detonation rocket engines for space propulsion, J. Propul. Power **37**, 463 (2021).

[44] D. Schwer and K. Kailasanath, Numerical investigation of the physics of rotating-detonation-engines, Proc. Combust. Inst. **33**, 2195 (2011).
[45] F. Zhang, S. B. Murray, and K. B. Gerrard, Aluminium dust-air detonation at elevated pressures, in *Shock Waves: Proceedings of the 24th International Symposium on Shock Waves*, edited by Z. Jiang (Springer, Berlin, Heidelberg, 2005), pp. 795–800.
[46] Q. Liu, X. Li, and C. Bai, Deflagration to detonation transition in aluminum dust–air mixture under weak ignition condition, Combust. Flame **156**, 914 (2009).
[47] Q. Liu, C. Bai, L. Jiang, and W. Dai, Deflagration-to-detonation transition in nitromethane mist/aluminum dust/air mixtures, Combust. Flame **157**, 106 (2010).
[48] W. A. Strauss, Investigation of the detonation of aluminum powder-oxygen mixtures, AIAA J. **6**, 1753 (1968).
[49] P. Zhang, Y. F. Zhang, Z. Chen, and H. Zhang, Combustion of micro aluminum particle suspension behind an incident shock wave, Int. J. Multiphase Flow **194**, 105429 (2025).
[50] G. J. Sharpe, Transverse waves in numerical simulations of cellular detonations, J. Fluid Mech. **447**, 31 (2001).
[51] M. D. Frederick, R. M. Gejji, J. E. Shepherd, and C. D. Slabaugh, Reactive transverse waves in a near-limit detonation, J. Fluid Mech. **1017**, A10 (2025).
[52] A. V. Fedorov and T. A. Khmel', Numerical simulation of formation of cellular heterogeneous detonation of aluminum particles in oxygen, Combust. Explos. Shock Waves **41**, 435 (2005).
[53] H. Hosoda, A. K. Hayashi, and E. Yamada, Numerical analysis on combustion characteristics of nano aluminum particle-oxygen two-phase detonation, Sci. Technol. Energ. Mater. **74**, 34 (2013).
[54] A. Briand, B. Veyssiere, and B. A. Khasainov, Modelling of detonation cellular structure in aluminium suspensions, Shock Waves **20**, 521 (2010).
[55] K. Benkiewicz and K. Hayashi, Two-dimensional numerical simulations of multi-headed detonations in oxygen-aluminum mixtures using an adaptive mesh refinement, Shock Waves **12**, 385 (2003).
[56] A. R. Kasimov and A. R. Gonchar, Reactive Burgers model for detonation propagation in a non-uniform medium, Proc. Combust. Inst. **38**, 3725 (2021).
[57] H. Shen and M. Parsani, The role of multidimensional instabilities in direct initiation of gaseous detonations in free space, J. Fluid Mech. **813**, R4 (2017).